

## Strain evolution after fiber failure in a single-fiber metal matrix composite under cyclic loading

Jay C. Hanan<sup>a,\*</sup>, Sivasambu Mahesh<sup>b</sup>, Ersan Üstündag<sup>a</sup>, Irene J. Beyerlein<sup>c</sup>,  
Geoffrey A. Swift<sup>a</sup>, Bjørn Clausen<sup>a</sup>, Donald W. Brown<sup>b</sup>, Mark A.M. Bourke<sup>b</sup>

<sup>a</sup> Department of Materials Science, California Institute of Technology, Pasadena, CA 91125, USA

<sup>b</sup> Materials Science and Technology Division, Los Alamos National Laboratory, Los Alamos, NM 87545, USA

<sup>c</sup> Theoretical Division, Los Alamos National Laboratory, Los Alamos, NM 87545, USA

### Abstract

The evolution of in situ elastic strain with cyclic tensile loading in each phase of a single  $\text{Al}_2\text{O}_3$ -fiber/aluminum-matrix composite was studied using neutron diffraction (ND). An analytical model appropriate for metal matrix composites (MMCs) was developed to connect the measured axial strain evolution in each phase with the possible micromechanical events that could occur during loading at room temperature: fiber fracture, interfacial slipping, and matrix plastic deformation. Model interpretation showed that the elastic strain evolution in the fiber and matrix was governed by fiber fracture and interface slipping and not by plastic deformation of the matrix, whereas the macroscopic stress–strain response of the composite was influenced by all three. The combined single-fiber composite model and ND experiment introduces a new and quick engineering approach for qualifying the micromechanical response in MMCs due to cyclic loading and fiber fracture.

© 2005 Elsevier B.V. All rights reserved.

**Keywords:** Metal matrix composites; Neutron diffraction; Micromechanical events; Interface shear; Composite deformation; Fiber failure

### 1. Introduction

Nearly all predictive models for fiber composite failure, regardless of their level of sophistication, require knowledge of the deformation behavior of the composite phases. The deformation of individual phases in composites can differ significantly from their respective monolithic behavior. Consider a metal matrix composite (MMC) with ceramic fibers. Any differences between the in situ and ex situ deformation of the metal matrix could arise because of microstructural constraints, localized strain gradients as a result of phase boundaries or defects, thermal residual stresses, and changes in the microstructure by virtue of composite fabrication and consolidation. One example of this is provided by recent work by

He et al. [1]. They showed that in  $\text{Al}_2\text{O}_3/\text{Al}$  composites, the in situ matrix yield strength was significantly higher than the monolithic value and increased with decreasing local fiber spacing. This distinctive in situ behavior was attributed to reduced grain size and increased dislocation densities near the fiber surface. Likewise, the ex situ versus in situ fiber strength could be different. A degradation of in situ fiber strength, e.g. lower average strength and higher variability could be the result of fabrication-induced defects. Lastly, such MMCs have an interface region, an interphase, or a reaction zone between the fiber and matrix materials. It is important to consider this region as a third constituent owning properties distinct from the fiber and matrix. Naturally, the in situ behavior of an interface cannot be determined and in situ characterization necessarily involves inverse or iterative methods using an interpretive model.

The failure of fiber-reinforced composites is largely dominated by the nucleation and interaction of fiber fractures. Local deformation in response to a fiber fracture may involve matrix plasticity, interfacial debonding and slipping,

\* Corresponding author. Present address: Mechanical & Aerospace Engineering, Oklahoma State University, OK 74106, USA.  
Tel.: +1 918 594 8238.

E-mail addresses: jay.hanan@okstate.edu (J.C. Hanan),  
ersan@caltech.edu (E. Üstündag).

matrix creep or a combination of these mechanisms. Such complex cases have been analyzed in a number of polymer matrix composites [2,3], using micro Raman spectroscopy and in metal matrix composites (MMCs), using chromium fluorescence peizospectroscopy [1]. There are, however, very few complete in situ studies of damage evolution in MMCs where both the matrix and fibers could be investigated (see e.g. [4–6]). Spectroscopy techniques are not ideal for MMCs because micro Raman spectroscopy [7] requires transparent matrices and peizospectroscopy [8] and is a surface technique. X-ray and neutron diffraction are more advantageous for damage evolution studies in MMCs as they provide in situ strain data from all phases, and especially for neutrons, are much more penetrating (in the order of cm).

A single-fiber composite, containing at least one fiber fracture, can be an excellent tool for characterizing and understanding various damage evolution mechanisms. More traditional characterization techniques, which use such specimens are fiber pull-out, push-out, or fragmentation tests. The latter typically involves a rather complex statistical analysis for interpretation [9]. Fiber pull-out (or push-out) specimens often contain a large volume fraction of matrix (approximately 80–99%); much larger than that found in real composites.

Therefore, microstructural constraints mentioned earlier may not exist in such specimens. Furthermore, in most of the above-mentioned tests substantial statistical variation in the estimates of the interfacial shear stress renders some of the results inconclusive.

There are a few analytical models, which analyze interface or matrix damage from a single broken fiber under cyclic loading [10,11]). However, these models are based on the shear lag concept, which assumes that the matrix deforms only in shear. While quite promising for composites with high-fiber volume fractions (over 60%), they are not applicable for the composite considered in this study (which had 33% fiber volume fraction). In this case, and for MMCs in general, it is essential that the axial deformation of the matrix is included in the analysis. The impact of residual stresses on local deformation, propagation and shrinkage of the plastic regions around the break, and macroscopic composite deformation will largely be governed by both shear and axial deformation in the matrix. Therefore, for reliable characterization of the interface and matrix properties, the interpretative model must allow for a combination of interface slip and matrix axial deformation.

The present work is concerned with characterizing the in situ matrix and interface deformation in a single-fiber MMC using neutron diffraction (ND). We studied the effects of in situ fiber fracture, matrix plasticity and interface slip on the elastic strain evolution observed with ND in both the fiber and matrix. The ND data were complemented with macroscopic stress–strain measurements which described the overall composite behavior. A new approach was developed that relates ND data to a simple, analytical model which tracks damage evolution in an  $\text{Al}_2\text{O}_3$ -fiber/Al-matrix composite under

cyclic loading. The model presented here did consider the axial deformation of the matrix, which was necessary for the correct interpretation of the deformation mechanisms.

## 2. Experimental procedure

### 2.1. Sample processing

A model composite comprised of a single, polycrystalline  $\text{Al}_2\text{O}_3$  fiber (4.75 mm diameter, from Coors Ceramics, Golden, CO, USA) and an Al matrix were prepared by casting. The Al alloy used was 6061 (ESPI Metals, Agoura Hills, CA, USA). The manufacturer reported an average grain size of 7  $\mu\text{m}$  in the fiber. The average grain size in the matrix was determined to be 21  $\mu\text{m}$  using the linear intercept method [12,13].

In order to ensure a fiber fracture at the center of the gage section during subsequent loading, a 0.4 mm notch was cut around the circumference of the fiber to a depth of 1.1 mm using a diamond saw. The sample was cast in a 304 stainless steel mold under vacuum after purging the mold with argon. The mold was machined to hold the alumina fiber vertically in a tube furnace while the Al melted around the fiber. Following 30 min at 800 °C, the entire mold was quenched in water at room temperature. A cylindrical tensile sample was then machined from the cast form. The final dimensions of the composite gave a 30 mm long gage length with an 8.25 mm gage diameter and 76 mm total sample length (Fig. 1). These dimensions yielded 33% fiber volume fraction for this specimen in the gage section.

To verify the fiber and interface integrity following casting and machining, X-ray radiography was performed using a Philips Dens-O-Mat at 65 kV and 7.5 mA. It was shown that the matrix did not contain noticeable voids within an estimated resolution of 30  $\mu\text{m}$  and the fiber was aligned with

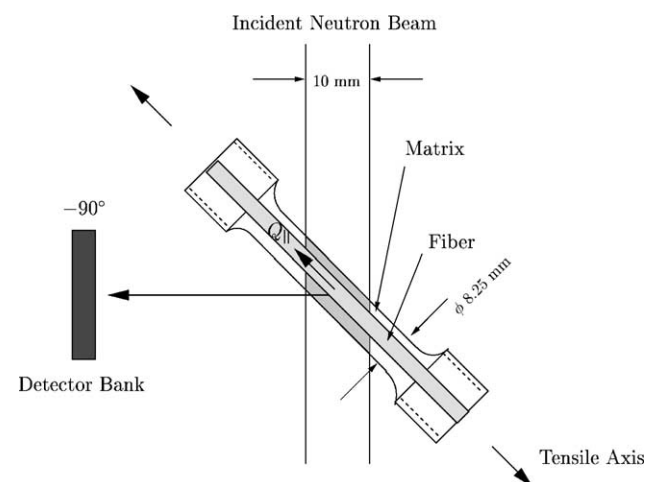


Fig. 1. Schematic of the single-fiber composite test during neutron diffraction. Longitudinal strains measured in the  $2\theta = -90^\circ$  detector bank were integrated over the volume irradiated by the incident neutron beam.

the central axis of the specimen. The specimen was also radiographed following the neutron diffraction experiments.

Another composite, prepared using the same method as mentioned above, had its matrix polished away from the fiber along a 30 mm region of the gage section. This fiber became free of the thermal residual stress that could be generated due to differences in its coefficient of thermal expansion with that of the matrix and was used as a strain-free reference for diffraction experiments. This way, the initial thermal residual strains for the fiber in the composite could be determined. A monolithic matrix alloy specimen was also processed similarly and used as a strain-free reference for the matrix.

## 2.2. Neutron diffraction experiments

Mechanical loading with simultaneous neutron diffraction was performed using the Neutron Powder Diffractometer (NPD) and the Spectrometer for Materials Research at Temperature and Stress (SMARTS) [14], both at the Los Alamos Neutron Science Center (LANSCE). Special hydraulic load frames stressed the samples in 10–20 MPa intervals for approximately, 45 min per loading step starting at 3 MPa.

Five tensile loading–unloading cycles were applied to the composite. In the first cycle, it was loaded to 80 MPa and unloaded to 3 MPa. In the subsequent cycles, it was loaded to 100 MPa and unloaded back to 3 MPa. Several neutron measurements were conducted during these cycles. During the fifth cycle, the specimen failed near the shoulder of its threaded section and outside the gage region sampled by diffraction. The sample was maintained in position after failure and final residual strain values were recorded:  $+460 \times 10^{-6}$  in the fiber and  $-740 \times 10^{-6}$  in the matrix. Post-mortem X-ray radiography of the composite showed that the fiber had also broken at the notch in the middle of the gage section.

Tensile stress during diffraction was also applied to the reference fiber sample to observe its mechanical response in monolithic form. The fiber was stressed in 20 MPa intervals up to 160 MPa while recording neutron diffraction patterns at the same time. The tensile stress–strain curve of the reference matrix sample was determined at Caltech using a screw-driven load frame. The axial macroscopic (total) strain in all three samples was monitored with a 25 mm gage length extensometer. Results showed that the matrix was linear elastic with a Young's modulus of 70 GPa until it reached its initial yield point of 80 MPa. Thereafter, the stiffness was reduced to 6 GPa. The fiber Young's modulus was measured to be 330 GPa.

Using time-of-flight neutron diffraction, the bulk average elastic lattice strain in the specimens was obtained in both the longitudinal and transverse directions simultaneously. A schematic revealing the loading and diffraction geometries is shown in Fig. 1. As indicated by the orientation of the scattering ( $Q$ ) vector, data from the  $2\theta = -90^\circ$  bank provided longitudinal (axial) strain information from both the fiber and

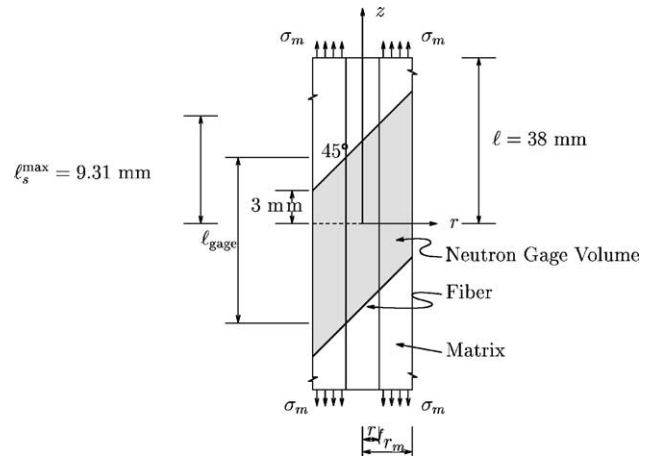


Fig. 2. Geometry of the test specimen and the neutron gage volume,  $r_f$  and  $r_m$  denote the fiber and composite radii, respectively. The maximum  $\epsilon_s$  calculated from the model, ( $\epsilon_s^{\max}$ ) is also shown. Stress is applied only to the matrix as indicated.

the matrix. It is important to note that the measured strains were an average over the 14 mm neutron gage length created by a 10 mm wide neutron beam, which illuminated the entire cross-section of the composite at an angle of  $45^\circ$ . This gage volume is illustrated in Fig. 2 as the grey shaded area.

The diffraction data were analyzed using the Rietveld method [15,16]. Comparison of the initial values of the lattice parameters of each phase of the composite to those obtained from the two reference monolithic samples showed that the thermal residual strains were relaxed in the composite to within  $200 \times 10^{-6}$  strain. This value is typical for strain error in neutron diffraction experiments that involve sample changes and is attributed to the sample displacement error [17]. Therefore, the reference point for the lattice strains due to applied loading was taken to be the nominally zero load position (at 3 MPa applied stress). The elastic strain in the Al matrix was calculated from changes in its lattice parameter. The cubic crystal structure of Al (space group  $Fm\bar{3}m$ , face centered cubic), its relatively low elastic anisotropy ( $=1.2$ ), and the effective averaging done by the whole-pattern Rietveld refinement justified this approach. However, the alpha alumina fiber had trigonal crystal structure (space group  $R\bar{3}c$ , corundum) and was somewhat textured. This led to an anisotropic (though linear) response by its  $a$ - and  $c$ -lattice parameters to applied loading. Furthermore, the relatively low intensity of  $00l$ -type reflections led to higher fitting errors in the  $c$ -lattice parameter. Therefore, the polycrystalline average of the Young's modulus of the fiber ( $=330$  GPa, determined by the extensometer during diffraction experiments on the reference fiber) was used to "adjust" the lattice strain exhibited by the  $a$ -lattice parameter so that it would represent the polycrystalline average. This approach was taken due to lack of detailed information about the texture in the fiber and to avoid making sweeping assumptions about load sharing among various lattice planes of alumina (see [18] for a related discussion).

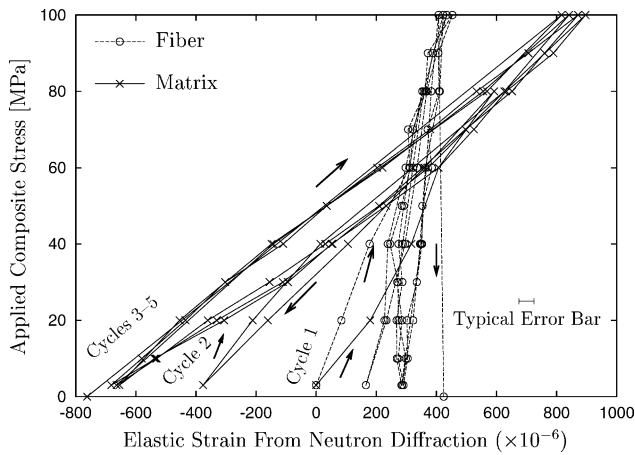


Fig. 3. Axial strains measured by neutron diffraction in each phase vs. applied composite stress during all the loading–unloading cycles for the composite specimen. The error bar represents a typical fitting error of  $\pm 25 \times 10^{-6}$  obtained during the experiment. Note that this value is much lower than that realized when sample change occurs (about  $\pm 200 \times 10^{-6}$ ).

### 3. Experimental results

Fig. 3 exhibits the axial lattice strain evolution in the composite during several loading–unloading cycles. The residual strains shown in this figure (at the end of each unloading cycle) experience a gradual evolution in both the matrix and the fiber. The matrix is seen to develop a progressively increasing compressive residual strain while the fiber attains higher tensile strain. This evolution is especially pronounced in the first three cycles and tends to saturate in the last two. This suggests that inelastic deformation no longer evolves beyond cycle 3.

Another important observation from Fig. 3 is the change in the apparent (diffraction) moduli of each phase given by the slope of applied composite stress versus elastic strain plots. To clearly see where these changes initiate, Fig. 4 shows

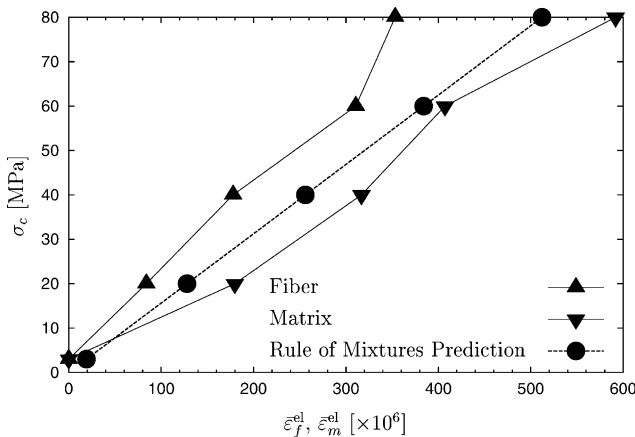


Fig. 4. The measured elastic strain in the fiber and matrix averaged over the neutron gage volume in the loading part of cycle 1. Also plotted is the rule of mixtures prediction of strain given by Eqs. (1)–(3).

the lattice strain evolution for just the loading portion of the first cycle. Even at the beginning, both phases evolve separately but appear to exhibit similar diffraction moduli until 60 MPa. Above this applied stress, the diffraction moduli of the matrix and fiber deviate further. As shown in Fig. 3, the matrix diffraction modulus decreases continuously and saturates around 74 GPa in cycles 3–5. At the same time, the fiber diffraction modulus increases from cycle 1 to 2 and does not change significantly in the remaining cycles until failure.

### 4. Analysis

The purpose of the following analysis is to associate the experimental strain data with a model that describes the mechanical behavior and interactions of the fiber, matrix, and interface. Since X-ray radiography of the composite did not reveal any voiding or cracking in the matrix, it was assumed that the most important aspects to consider in the model were fiber fracture, matrix plasticity and interfacial shear response. The preliminary analysis in Section 4.1 shows that the fiber–matrix interface was not intact during the cyclic loading. Based on this result, a simple analytical model with an elastic fiber, a slipping interface, and an elastoplastic matrix was developed and will be described in Section 4.2.

The material data used in the following calculations are shown in Table 1. The alumina fiber was assumed to be elastic throughout, with a modulus of 330 GPa, as measured in the tension test of the reference fiber. A linear hardening law was fit to the matrix alloy's monolithic stress–strain curve in tension (fit not shown). The initial yield point was 80 MPa and the resulting values for the stiffness of the monolithic matrix in the elastic ( $E_m$ ) and plastic ( $E'_m$ ) regions are listed. In what follows, relative displacement of the fiber and matrix across the interface will be called interfacial slipping.

#### 4.1. Intact interface

This section establishes that the fiber–matrix interface in the composite specimen was not intact, i.e., it experienced slipping during tensile loading. An estimate of the uniform stresses and strains far from specimen ends in the fiber ( $\sigma_f^{r.o.m.}$ ) and matrix ( $\sigma_m^{r.o.m.}$ ), when both of these are

Table 1

Material parameters for the matrix and interface used in the modeling calculations

Measured			Estimated	
$E_m$ (GPa)	$E'_m$ (GPa)	Yield point (monolith) (MPa)	$\tau_s$ (MPa)	Yield point, $\sigma_Y$ (in situ) (MPa)
70	6	80	55	80

The first three were obtained from the tension test of the monolithic matrix sample while the last two are in situ parameters in the composite estimated by the model.



elastic and well bonded, is given by the rule of mixtures as:

$$\sigma_f^{r.o.m.} = \frac{\sigma_c(A_f + A_m)E_f}{E_f A_f + E_m A_m} \quad (1)$$

and

$$\sigma_m^{r.o.m.} = \frac{\sigma_c(A_f + A_m)E_m}{E_f A_f + E_m A_m} \quad (2)$$

Here,  $\sigma_c$  is the applied composite stress, while  $A_f$  and  $A_m$  denote the cross-sectional areas of the fiber and matrix, respectively. The elastic strain in the fiber ( $\varepsilon_f^{r.o.m.}$ ) and matrix ( $\varepsilon_m^{r.o.m.}$ ), however, are equal:

$$\varepsilon_f^{r.o.m.} = \varepsilon_m^{r.o.m.} = \frac{\sigma_f^{r.o.m.}}{E_f} = \frac{\sigma_m^{r.o.m.}}{E_m} \quad (3)$$

Chen et al [19] have studied an alumina fiber/6061 aluminum alloy matrix composite with an intact fiber and a strong interface obtained by a fabrication procedure different from that used in this work. They found that the experimental composite moduli matched those derived from rule of mixtures considerations.

Fig. 4 shows the elastic strain evolution in the present specimen in both phases during cycle 1 along with the rule of mixtures curve. If the fiber were intact, the fiber and matrix were elastic and well-bonded, and the (neutron) gage volume sufficiently removed from the ends of the specimen where load was applied, then the strain in the gage volume would be uniform and the fiber and matrix would experience the same strain as that predicted by the rule of mixtures. However, it is seen that fiber and matrix strains fall to either side of the rule of mixtures line (Fig. 4). Because of this deviation, we can conclude that the fiber and matrix are neither deforming elastically nor well bonded.

A possible mechanism to consider when interpreting the observed behavior in Fig. 4 is matrix yielding while the interface remained intact. Selecting an intermediate stress level  $\sigma_c = 40$  MPa for Eqs. (1) and (2), the following stress values are obtained:  $\sigma_f^{r.o.m.} \approx 92$  MPa and  $\sigma_m^{r.o.m.} \approx 15$  MPa. Both of these values are well below the monolithic yield points of the fiber and matrix; therefore, both phases would likely remain elastic if the fiber and interface were both intact. Even if the matrix did yield (perhaps due to either a very low in situ yield stress or a high tensile thermal residual stress prior to loading) while the interface was intact, the experimental data would not be matched by the rule of mixtures model. For in that case, the fiber and matrix strains would evolve instead as illustrated in Fig. 5. As shown, the matrix would become compliant due to plasticity and transfer more load to the fiber through the interface than that predicted by the rule of mixtures formula. Accordingly, the fiber strain would exceed the rule of mixtures value and the matrix strains would fall below the rule of mixtures value. However, the opposite is observed in Fig. 4. The measured elastic strain in the fiber is smaller than the rule of mixtures value and the elastic strain in the matrix is consistently larger than the rule of mixtures prediction. It was, therefore, concluded that the reason for

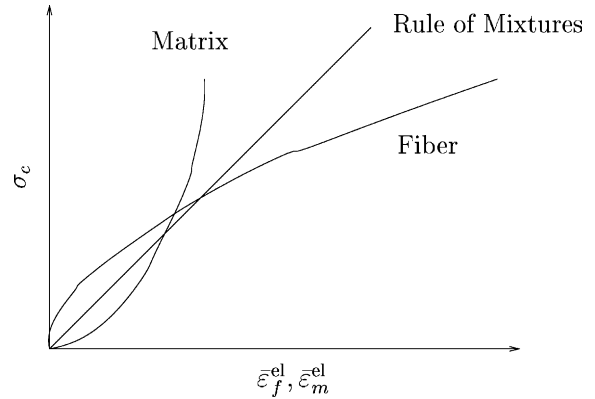


Fig. 5. Schematic representation of the expected stress–strain response in a composite with an intact fiber, a bonded interface and a yielding matrix.

the observed strain evolution in both phases was inefficient load transfer from the matrix to the fiber due to slipping at the interface.

Another indication of slipping at the interface is furnished by the discrepancy in the residual strains after specimen fabrication. It was reported in Section 2.2 that the measured average thermal residual strain in the specimen is small, and comparable to the experimental error of measurement. We used an axis-symmetric finite element (FE) calculation to compute the thermal residual state in a specimen cooled by 100 K from a stress-free state. In choosing the stress-free temperature to be 100 K above room temperature, we are guided by the work of Fukui and Watanabe [20] on an alloy similar to the present matrix material (albeit with SiC particle reinforcements). They find that the thermal residual stress in their material is well-modeled by their theory if the stress-free temperature is taken as 140 K above room temperature. In order to be sure of underestimating the residual elastic strains, we round this down to 100 K above room temperature.

In the FE calculation, we assumed an intact elastic fiber, an isotropically hardening matrix whose stress–strain curve is set to the measured bulk response of the matrix material, and a perfectly bonded interface. We took the coefficient of thermal expansion of the aluminum matrix to exceed that of the alumina fiber by  $12 \times 10^{-6}/K$ , independent of temperature. The FE results yield elastic strains much more than what is measured. The calculated elastic axial strain at  $r=r_f$  is approximately  $790 \times 10^{-6}$ , while that near  $r=r_m$  is approximately  $330 \times 10^{-6}$ . These values remain nearly constant in the neutron gage volume, away from the specimen ends. The gage volume average of the axial elastic strain must fall between these extremes. Since the measured value lies far lower, it suggests that an assumption of the model, viz. compatibility at the interface is being violated in the experiment.

It must also be mentioned that the above residual strain computation could have alternatively been performed using simple concentric cylinder models (see Johnson et al. [21]).

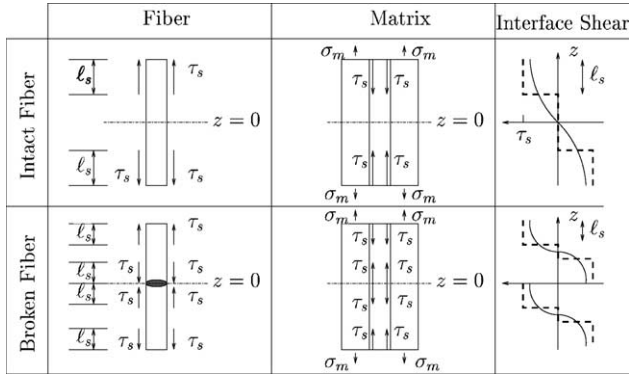


Fig. 6. Free body diagrams showing the idealized stresses in the fiber and matrix with a slipping interface. Two cases are considered: the first row shows an intact fiber and the second, a broken fiber. Column 3 schematically compares the likely actual interfacial shear profile (solid) to the shear profile idealized in the present model (dashed).

#### 4.2. Slipping interface: elastic strain evolution

In this section, we use a simple analytical model to gain a first understanding of the evolution of elastic (lattice) strains in both the matrix and fiber. A key assumption on the interfacial shear stress profile underlies the simplicity of the model. Below, we describe the model with its assumptions and then examine their validity and consequences. Fig. 2 shows a schematic of the sample geometry around the neutron gage section. The assumed interactions between the fiber and matrix are modeled as shown in the free body diagrams of Fig. 6. Two cases of interest are the events before and after fiber fracture; these occupy respectively, the first and second rows of the figure. The figure also shows two of the unknown parameters in the model:  $\tau_s$  and  $l_s(\sigma_c)$ , which quantify the model interfacial shear profile shown. The latter is a function of the applied stress ( $\sigma_c$ ) while the former is not. The  $l_s(\sigma_c)$  in the  $z$ -axis is the same within the same row. Equilibrium dictates that  $l_s(\sigma_c)$  be equal near traction-free fiber ends, both in the intact and broken fiber cases. It is critical to realize that by assuming the shear stress profile as shown in the last column of Fig. 2, the original problem reduces to two axis-symmetric traction boundary value problems, one each for the fiber and matrix, which can be readily solved for elastic strains even though the matrix may be undergoing plastic deformation. This is because the traction boundary conditions shown in Fig. 6 together with equilibrium considerations determine the stress, and hence, the elastic strain state, independent of the constitutive law.

In actuality, the interfacial shear profile is determined by displacement compatibility across the interface where the shear stress is below a certain frictional threshold, and equals the frictional shear-stress threshold elsewhere. A schematic sketch of the actual and assumed shear-stress profiles is shown for the broken and intact fiber cases in the third column of Fig. 6. Note that by symmetry, the shear stress must be zero at  $z=0$  when the fiber is intact and at  $z=\pm l/4$  when a fiber

break is present at  $z=0.2l$ ;  $l$  is half the length of the specimen (see Fig. 2). By fitting  $\tau_s$ , and  $l_s(\sigma_c)$  to the experimental elastic strain data, the present model only aims to capture the correct amount of load transfer from matrix to fiber, and thereby to capture the axial elastic strains in the neutron gage volume.

We caution that  $\tau_s$  should not be interpreted as an approximation of the actual critical interfacial shear stress, nor  $l_s(\sigma_c)$  as the actual interfacial slip length. These interpretations will only hold if the actual interfacial shear profile is well approximated by the assumed shear profile, and we are unable to assert that using the present model. In other words, good approximations of the critical interfacial shear stress and slip length fall outside the scope of the present model and are left to future modeling work to determine. However, a permissible interpretation is that  $\tau_s l_s(\sigma_c)/l_{\text{gage}}$ , where  $l_{\text{gage}}$  is the length of the interface within the neutron gage volume (see Fig. 2) approximates the actual average interfacial shear stress over the length of the interface within this volume.

We make some further assumptions before proceeding. Because only a few loading cycles are considered, interface degradation is expected to be minimal, and therefore, we assume  $\tau_s$  is constant while fitting all cycles of the experiment. The applied stress at the grips is represented by a uniform tensile stress of  $\sigma_m = \sigma_c (A_f + A_m)/A_m$  acting at each end of the matrix (see Fig. 2). Finally, normal (radial) stresses between the fiber and matrix are ignored. Therefore, the axial strains arising from the Poisson effect are not considered in comparison to the axial strains due to axial loading.

Using one-dimensional equilibrium considerations along the fiber axis ( $z$  direction) for the intact fiber case (the first row of Fig. 6), the fiber stress was obtained as:

$$\sigma_f(z) = \begin{cases} \frac{2\tau_s l_s}{r_f}, & \text{if } 0 \leq |z| \leq l - l_s \\ \frac{2\tau_s(l - z)}{r_f}, & \text{if } l - l_s \leq |z| \leq l, \end{cases} \quad (4)$$

where  $2l$  is the total length of the composite. As marked in Fig. 2,  $l = 38$  mm,  $r_f$  and  $r_m$  are the fiber radius and outer radius, respectively, and  $z$  is the fiber axial coordinate defined from the notch. Similarly, the matrix stress was given by:

$$\sigma_m(z) = \begin{cases} \frac{\sigma_c r_m^2 - 2\tau_s l_s r_f}{r_m^2 - r_f^2}, & \text{if } 0 \leq |z| \leq l - l_s \\ \frac{\sigma_c r_m^2 - 2\tau_s(l - z)r_f}{r_m^2 - r_f^2}, & \text{if } l - l_s \leq |z| \leq l \end{cases} \quad (5)$$

Following the same approach for the broken fiber case (the second row of Fig. 6), the fiber and matrix stresses were:

$$\sigma_f(z) = \begin{cases} \frac{2\tau_s z}{r_f}, & \text{if } 0 \leq |z| \leq l_s \\ \frac{2\tau_s l_s}{r_f}, & \text{if } l_s \leq |z| \leq l - l_s \\ \frac{2\tau_s(l - z)}{r_f}, & \text{if } l - l_s \leq |z| \leq l, \end{cases} \quad (6)$$

and

$$\sigma_m(z) = \begin{cases} \frac{\sigma_c r_m^2 - 2\tau_s z r_f}{r_m^2 - r_f^2}, & \text{if } |z| \leq l_s \\ \frac{\sigma_c r_m^2 - 2\tau_s l_s r_f}{r_m^2 - r_f^2}, & \text{if } l_s \leq |z| \leq l - l_s \\ \frac{\sigma_c r_m^2 - 2\tau_s (l - z) r_f}{r_m^2 - r_f^2}, & \text{if } l - l_s \leq |z| \leq l \end{cases} \quad (7)$$

For both cases, the one-dimensional Hooke's law gave the elastic strains as:

$$\varepsilon_f^{\text{el}}(z) = \frac{\sigma_f(z)}{E_f}, \text{ and} \quad (8)$$

$$\varepsilon_m^{\text{el}}(z) = \frac{\sigma_m(z)}{E_m}$$

To compare with the neutron measurements, all calculated strains were averaged over the neutron gage volume, which was asymmetric, as illustrated in Fig. 2. Eqs. (4)–(8) involve two unknowns:  $\tau_s$  and  $l_s$ . Following the procedure detailed below,  $\tau_s$  and  $l_s(\sigma_c)$  were refined, so that the calculated average matrix strains agreed well with the neutron diffraction data. The success of the model was judged by the agreement between the measured and predicted fiber strains.

As Eqs. (5), (7), and (8) indicate, the axial strain in the matrix has a linearly decreasing region near the fiber-free surfaces and a region of uniform strain in between. A larger  $\tau_s$  implies more rapid load transfer between the fiber-aid matrix, i.e., a smaller  $l_s(\sigma_c)$  for all  $\sigma_c$ . For fixed  $\tau_s$ , by adjusting  $l_s(\sigma_c)$  it was, therefore, possible to alter the averaged elastic strain over the neutron gage volume. From Fig. 3, it is observed that the measured, average, elastic fiber strain ( $\bar{\varepsilon}_f^{\text{el}}$ ) is sensitive to  $\sigma_c$ . According to Eqs. (4) and (6), however, the model predictions of this strain should be independent of  $\sigma_c$  if  $l_s(\sigma_c)$  were to approach or exceed the neutron gage length

of the fiber. This observation supplied us with the following constraint on the choice of  $\tau_s$ :  $\tau_s$  was required to be large enough, so that  $l_s(\sigma_c)$  would always be contained within the neutron beam. Therefore, for a given  $\tau_s$  within this range one can choose a suitable  $l_s(\sigma_c)$  to fit the measured matrix strains with the model predictions. The value of  $\tau_s$ , and its associated  $l_s(\sigma_c)$  were selected based on the one that best predicted the measured fiber strain.

Next, within this range of  $\tau_s$  an iterative calculation was performed in which  $\tau_s$  was varied to obtain the best agreement between the measured and calculated fiber strains. Note that this was a one-parameter ( $\tau_s$ ) fit of the fiber profile and did not amount to fitting the fiber curve in the same sense as fitting the matrix curve. Furthermore,  $\tau_s$  can only be varied over a limited range as described above. This involved fitting  $l_s(\sigma_c)$ , each time  $\tau_s$  was altered to continue to fit the matrix strains. The calculations showed that the calculated  $\bar{\varepsilon}_f^{\text{el}}$  always exceeded the measured  $\bar{\varepsilon}_f^{\text{el}}$ . Therefore, the best choice of  $\tau_s$  was determined by the aforementioned constraint;  $\tau_s = 55$  MPa was the smallest value such that the  $l_s$  remained within the beam.

Figs. 7 and 8 compare the calculated and measured average elastic strains in the first and second loading cycles of the composite, respectively. The prediction used  $\tau_s = 55$  MPa and its associated  $l_s(\sigma_c)$ . The  $l_s(\sigma_c)$  used for the fit are shown in Fig. 9.  $l_s(\sigma_c)$  progressively increases with higher applied stress and reaches its maximum value ( $=9.31$  mm) in cycle 3 at  $\sigma_c = 100$  MPa. The residual value of  $l_s(\sigma_c)$  (at  $\sigma_c = 3$  MPa) also increases slowly with successive cycles suggesting a slow degradation of the interface with continued cyclic loading of the composite.

The model is only slightly sensitive to the value of  $\tau_s$ . Setting  $\tau_s = 60$  MPa, and refitting  $l_s(\sigma_c)$  so as to align the calculated and measured average matrix strains results in an increase of only  $4 \times 10^{-6}$  in the computed average fiber strain at the peak load of 80 MPa during cycle 1. The corresponding increase in cycle 2 is  $17 \times 10^{-6}$ . The computed average fiber

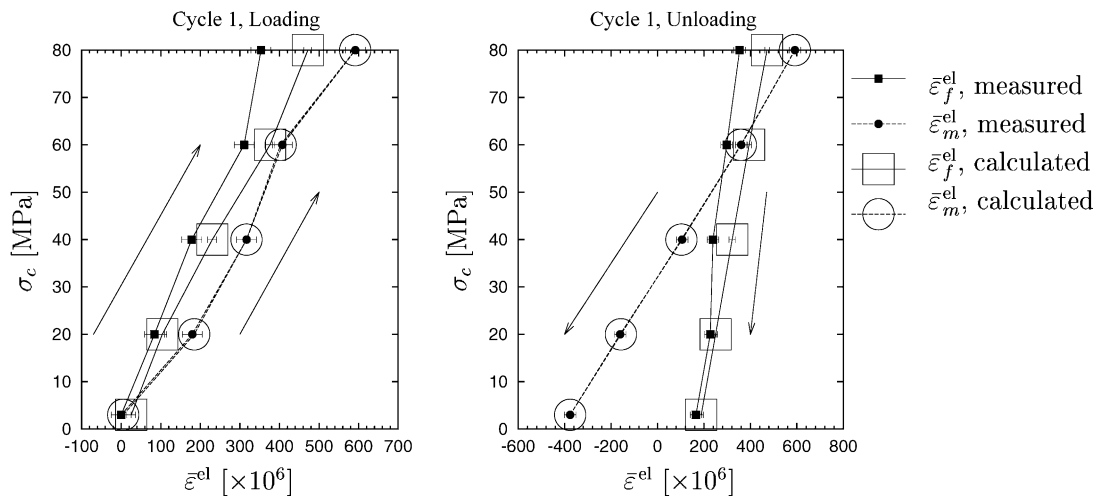


Fig. 7. Comparison of the measured and calculated volume averaged lattice strains in cycle 1 of the composite assuming that the fiber failed in this cycle. The model is fit to the matrix curve and is used to calculate the fiber curve, which is seen to be in good agreement with the measured fiber strains.

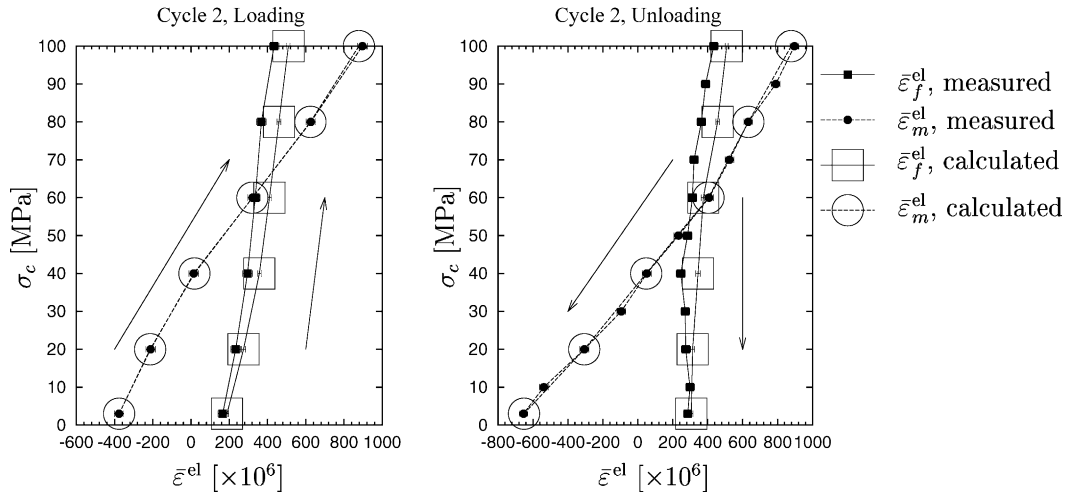


Fig. 8. Comparison of the measured and calculated volume averaged lattice strains in cycle 2 of the composite. The fiber was assumed to fail during cycle 1. The model is fit to the matrix curve and is used to calculate the fiber curve, which is seen to be in good agreement with the measured fiber strains.

residual strain after cycle 2 remains unchanged when  $\tau_s$  is changed from 55 to 60 MPa.

It is generally accepted that  $\tau_s$  may decrease substantially during the first few cycles of loading, as the asperities leading to friction at the interface are ground down during load cycling [22,23]. Using the present simple model, although we are unable to firmly deduce such a lowering of  $\tau_s$  with load cycling, or lack thereof, we have grounds to believe that any such reduction is small in our specimen. Because, according to the model,  $\tau_s = 55$  MPa leads to a maximum  $l_s = 9.31$  mm in the third cycle, that is, only slightly less than quarter the length ( $l/2$ ; see Fig. 2) of the composite. Since physically,  $l_s \leq l/4$ , the actual  $\tau_s$  during the third cycle cannot be much less than 55 MPa. Now, suppose that the value of  $\tau_s$  is larger than 55 MPa in the first two cycles. This contradicts the result of the preceding paragraph that the fits using  $\tau_s = 60$  MPa are poorer than those using  $\tau_s = 55$  MPa (albeit only slightly).

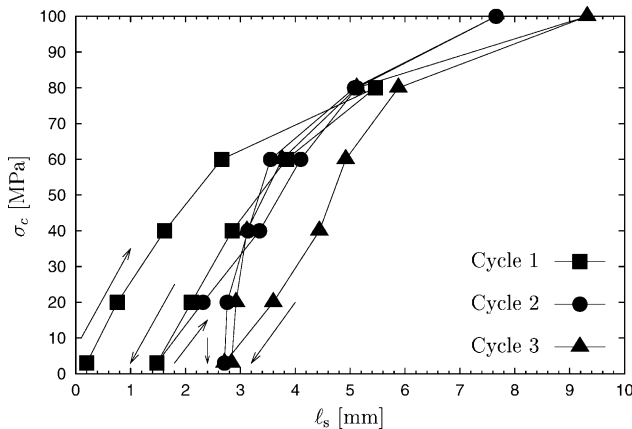


Fig. 9. The evolution of the model slip length  $l_s$  in the composite for  $T_s = 55$  MPa. The fiber was assumed to fracture between 60 and 80 MPa in cycle 1. These  $l_s$  values were used to generate the model predictions in Figs. 7 and 8.

Thus, even in the first two cycles, we suspect that  $\tau_s$  is not much more than 55 MPa in the experimental specimen.

Push-out and pull-out experiments are commonly used to characterize inter-facial  $\tau_s$ . While such experiments do not give a clear indication of the shear profile along the interface, an approximation of  $\tau_s$  is obtainable by assuming the inter-facial shear profile to be uniform and applying Kelly's [24] formula:

$$\tau_s \approx \frac{P}{2\pi a H} \quad (9)$$

where  $P$  is the peak load applied to the fiber,  $a$  its radius, and  $H$  its embedded length in the matrix,  $\tau_s$  depends sensitively on the fiber and matrix materials, composite-fabrication technique, testing temperature, among others. We are unaware of extensive interfacial studies through pull-out or push-out tests for our composite system. However, a detailed push-out study of SiC fiber–Al matrix interfaces was done by Lu et al [25], who found  $\tau_s$  to be a Weibull-distributed random quantity of fairly large variance, with average strength 60.9 or 46.8 MPa, depending on the composite fabrication procedure. Thus, the fit value  $\tau_s = 55$  MPa falls within a reasonable range.

The fiber was assumed to fracture between 60 and 80 MPa of cycle 1 in these calculations. While an X-ray radiograph of the specimen after the experiment did reveal a broken fiber, there is some uncertainty as to when exactly it broke during the experiment. Although a lower probability, the fiber might have also broken during cycle 2. If this were the case, then the fiber failure would have occurred between 80 and 100 MPa in this cycle because the sample faced no higher stresses in subsequent cycles. Separate calculations were performed (not shown here) for the second case of fiber fracture, also with  $\tau_s = 55$  MPa. The fiber strains were predicted to be within  $\pm 20 \times 10^{-6}$  of those estimated for the first case (fiber fracture during cycle 1). In either case, however, the main premise of this study is still valid; strain evolution during the



cyclic loading of this alumina/aluminum composite could be described reasonably well by a slipping interface model.

The success of the present simple model can be judged by comparing the calculated average strains in the fiber with those measured. The model reproduced the fiber elastic strain data within the error of measurement for small applied stresses and captured accurately the residual strain at the end of cycles 1 and 2 (Figs. 7 and 8). There was some discrepancy, however, between the data and model predictions at higher loads (the maximum strain deviation was  $118 \times 10^{-6}$  at  $\sigma_c = 80$  MPa in cycle 1). These deviations suggest a slight difference between the actual shear profile at the interface and that assumed by the model. Several kinks in the fiber strain data (e.g. at  $\sigma_c = 40$  MPa during unloading, in both cycles 1 and 2) support this hypothesis. These kinks were likely to be caused by some non-uniform slipping along the interface, contrary to the uniform slipping assumed by the proposed model. In conclusion, it is not possible to rule out some stick-slip-type behavior at the interface. Nonetheless, based on arguments presented earlier (see Section 4.1), it is clear that the composite behavior is better characterized by a uniformly slipping interface than an intact one.

#### 4.3. Slipping interface: plastic strain evolution

For a final validation of the slipping interface model, the total (elastic + plastic) surface strain in the composite as measured by the extensometer was compared to model predictions. Fig. 10 shows the evolution of the total axial surface strain in the matrix as a function of applied composite stress ( $\sigma_c$ ) during cycle 1 (with a maximum stress of 80 MPa) and cycle 2 (with a maximum stress of 100 MPa).

In this comparison, the tensile stress–strain curve of the monolithic matrix (not shown) was approximated as two

straight lines: linear elasticity with modulus  $E_m$  up to  $(\varepsilon_Y, \sigma_Y)$  followed by linear hardening with modulus  $E'_m$ :

$$\sigma_m(z) = \begin{cases} E_m \varepsilon_m(z), & \text{if } \varepsilon_m(z) < \varepsilon_Y \\ E'_m \varepsilon_m(z) + (E_m - E'_m) \varepsilon_Y, & \text{if } \varepsilon_m(z) \geq \varepsilon_Y \end{cases} \quad (10)$$

where  $\varepsilon_Y = \sigma_Y/E_m$  is the yield strain, and  $\sigma_Y$  is the yield stress. Therefore, for  $\sigma_m \geq \sigma_Y$ , the plastic part of the matrix strain during loading over the previous maximum stress is given by

$$\varepsilon_m^{pl}(z) = \sigma_m(z) - \sigma_Y \left( \frac{1}{E'_m} - \frac{1}{E_m} \right) \quad (11)$$

The material parameters obtained by fitting this equation to the stress–strain curve of the monolithic matrix are shown in (Table 1).

Knowing the matrix stress in the composite ( $\sigma_m(z)$ ) from Eqs. (4) to (7), the plastic part of the matrix strain could be computed from Eq. (11). Here,  $\varepsilon_m^{pl}(z)$  was only calculated during loading and above the previous maximum stress. The plastic strain was assumed to remain unchanged during unloading, i.e., the matrix was not expected to yield during this step. Note that in the above  $\sigma_Y$  can be considered an unknown, allowing for the possibility that the in situ yield stress is different than the ex situ one. The calculated total matrix strain is then  $\varepsilon_m^{tot} = \varepsilon_m^{el} + \varepsilon_m^{pl}$  as given by Eqs. (8) and (10) above.

The calculated and measured total strain in the matrix (i.e., at the surface of the composite) are compared favorably in Fig. 10. When the in situ matrix yield stress in the composite ( $\sigma_Y$ ) was treated as a fitting parameter, a value of 80 MPa gave the best fit. Interestingly, 80 MPa was also the yield point of the monolithic matrix specimen. This result suggests that the matrix had not undergone appreciable in situ hardening during quenching, possibly due to the poor interfacial constraint between fiber and matrix. This is also in agreement with the observation in Section 3 that the thermal residual stress in the matrix after quenching was small. All of these results confirm the poor quality of the fiber–matrix interface in the composite specimen.

## 5. Conclusions

Combined neutron diffraction and micromechanical modeling allowed the characterization of the in situ failure events occurring in an  $\text{Al}_2\text{O}_3/\text{Al}$  single-fiber composite under cyclic tensile loading. Neutron diffraction provided the necessary strain resolution to deduce the deformation characteristics of each phase. From the in situ strain evolution and the macroscopic stress–strain curve, it was evident that interface slipping, fiber fracture, and matrix yielding evolved during the first two cycles of the five-cycle test, with maximum stresses of 80 and 100 MPa, respectively. Significant changes in the composite's residual strains were associated with these failure events. Later, cycles with the same maximum stress of 100 MPa showed minimal irreversible deformation. The

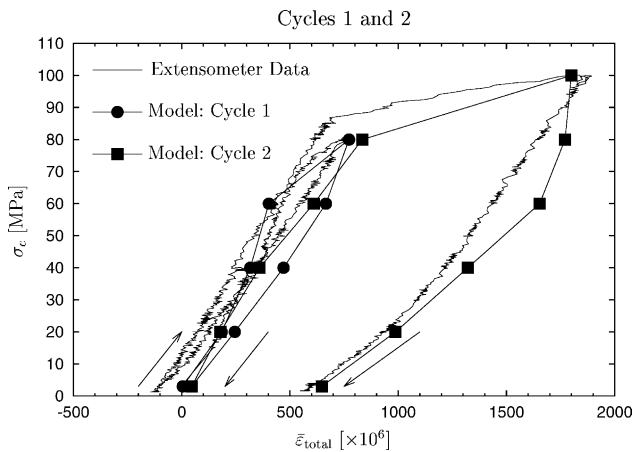


Fig. 10. Comparison of the measured and calculated total axial strains on the surface of the composite assuming the fiber broke in cycle 1. The experimental strain data were collected by a 25 mm gage length extensometer clamped symmetrically across the neutron sampling volume.

results also provided evidence that the fiber-sustained load in spite of a fiber fracture and interface degradation.

An analytical model was used to interpret the in situ interface and matrix behavior from the neutron diffraction results. Consistent with specimen geometry, the model considers a single-fiber composite allowing for axial matrix strain and interfacial slipping with or without a fiber fracture. The analysis accounted for the asymmetric neutron gage volume, and yielded good agreement with the experimental data. The interpretation of the model suggests that the elastic strain evolution of the fiber and matrix was governed by fiber fracture and interface slipping, whereas the macroscopic stress–strain response of the composite was also governed by the plastic deformation in the matrix. Possibly, due to the weak interface the in situ matrix yield stress was the same as that in monolithic form. This suggests that repeating the current studies using single-fiber composite specimens with a strong interface would certainly elucidate differences between the in situ and ex situ yield stresses.

The present analytical model does not account for compatible displacement across part of the interface, which would call for a displacement-based model of matrix plasticity and slip. A model, which accounts for matrix plasticity and slip over part of the interface (including reversals) is needed for a better analysis of the experiment and is presently being developed.

The methodology developed in this study provides a quick, yet powerful engineering tool to investigate the in situ damage evolution in fiber-reinforced composites, especially under cyclic loading. New capabilities now exist with neutron diffraction [14] that allows loading experiments at temperatures reaching 1500 °C. The approach presented here will be invaluable in quantifying matrix and interface behavior in high-temperature regimes. Work is in progress to achieve this and to exploit the new experimental capabilities and the improved methodology described above.

## Acknowledgements

Funding was provided by the National Science Foundation (CAREER grant no. DMR-9985264) at Caltech and a Laboratory-Directed Research and Development Project (no. 2000043) at Los Alamos. The neutron diffraction experi-

ments were conducted at the Lujan Center, LANSCE, a national user facility supported by the Department of Energy, Office of Basic Energy Sciences under contract W-7405-ENG-36. Dr. C. Brian Hooper assisted with the radiographic measurements.

## References

- [1] J. He, I.J. Beyerlein, D.R. Clarke, *J. Mech. Phys. Solids* 47 (1999) 465.
- [2] C. Zhou, L.S. Schadler, I.J. Beyerlein, *Acta Mater.* 50 (2002) 365.
- [3] I.J. Beyerlein, M.S. Amer, L.S. Schadler, S.L. Phoenix, *Sci. Eng. Compos. Mater.* 7 (1998) 151.
- [4] J.C. Hanan, E. Üstündag, B. Clausen, S. Mahesh, I.J. Beyerlein, D.W. Brown, M.A.M. Bourke, *Mater. Sci. Forum* 404–407 (2002) 907.
- [5] J.C. Hanan, G.A. Swift, E. Üstündag, L.I. Beyerlein, J.D. Almer, U. Lienert, D.R. Haefner, *Metall. Mater. Trans. A* 33A (2002) 3839.
- [6] J.C. Hanan, E. Üstündag, I.J. Beyerlein, G.A. Swift, J.D. Almer, U. Lienert, D.R. Haefner, *Acta Mater.* 51 (14) (2003) 4239–4250.
- [7] L.S. Schadler, C. Galotis, *Int. Mater. Rev.* 40 (1995) 116.
- [8] Q. Ma, M.C. Shaw, M.Y. He, B.J. Dalgleish, D.R. Clarke, A.G. Evans, *Acta Metall. Mater.* 40 (1995) 2137.
- [9] C.-Y. Hui, S.L. Phoenix, M. Ibnabdeljalil, R.L. Smith, *J. Mech. Phys. Solids* 43 (1995) 1551.
- [10] Y.C. Gao, L.M. Zjou, *Theor. Appl. Fracture Mech.* 28 (1997) 29.
- [11] J. Zhang, J. Wu, S. Liu, *Compos. Sci. Technol.* 62 (2002) 641.
- [12] W.D. Callister Jr., *Materials Science and Engineering, An Introduction*, third ed., John Wiley and Sons Inc., New York, 1994, p. 84.
- [13] ASTM: E112-88, *Standard Test Methods for Determining Grain Sizes*, pp. 297–322.
- [14] Bourke MAM, D.C. Dunand, E. Üstündag, *Appl. Phys. A* 74 (2002) S1707.
- [15] H.M. Rietveld, *J. Appl. Cryst.* 2 (1969) 65.
- [16] A.C. Larson, R.B. von Dreele, *GSAS-General Structure Analysis System*, LAUR, Los Alamos National Laboratory, 1986, pp. 86–748.
- [17] I.C. Noyan, J.B. Cohen, *Residual Stress: Measurement by Diffraction and Interpretation*, Springer Verlag, New York, 1987.
- [18] K. Tanaka, Y. Akiniwa, *JSME Int. J.* 41 (1998) 280.
- [19] A.S. Chen, R.S. Bushby, M.G. Phillips, V.D. Scott, *Proc. R. Soc. Lond. A* 450 (1995) 537.
- [20] Y. Fukui, Y. Watanabe, *Metall. Mater. Trans. A* 27A (1996) 4145.
- [21] W.S. Johnson, J.M. Larsen, B.N. Cox, *Life prediction methodology for Ti matrix composites*, ASTM STP 1253, American Society for Testing and Materials, W. Conshohocken, PA.
- [22] H. Teng, A. Agah-Tehrani, *J. Appl. Mech.* 59 (1992) 547.
- [23] H.Y. Liu, L.M. Zhou, Y.W. Mai, *Philos. Mag. A* 70 (1994) 359.
- [24] A. Kelly, *Proc. R. Soc. Lond. A* 319 (1970) 95.
- [25] Y. Lu, M. Hirohashi, J. Pan, H. Asanuma, *J. Mater. Sci. Lett.* 19 (2000) 1343.